J. Synchrotron Rad. (1999). **6**, 1051–1058

Local structure and mean-square relative displacement in SiO_2 and GeO_2 polymorphs

Akira Yoshiasa,[a]* Takuo Tamura,[b] Osamu Kamishima,[c] Kei-ichiro Murai,[a] Kiyoshi Ogata[b] and Hiroshi Mori[d]

[a]Graduate School of Science, Osaka University, Toyonaka 560, Japan, [b]Production Engineering Research Laboratory, Hitachi Ltd, Totsuka, Yokohama 244, Japan, [c]Research Institute for Scientific Measurements, Tohoku University, Sendai 980, Japan, and [d]Faculty of Science, Ehime University, Matsuyama 790, Japan. E-mail: yoshiasa@ess.sci.osaka-u.ac.jp

(*Received 18 January 1999; accepted 20 April 1999*)

Extended X-ray absorption fine structure (EXAFS) spectra near the Si and Ge *K*-edge for SiO_2 and GeO_2 polymorphs were measured in transmission mode with synchrotron radiation at the Photon Factory, Tsukuba. The local structures and mean-square relative displacements were determined in α-tridymite, α-quartz and stishovite. In stishovite, Si is octahedrally coordinated and the four coplanar Si—O bonds [1.755 (8) Å] are shorter than the other two axial bonds [1.813 (15) Å]. The high-temperature phase tridymite [1.597 (3) Å] has a smaller local bond distance than α-quartz [1.618 (5) Å]. The temperature variation of the local structural parameters for quartz-type GeO_2 (q-GeO_2) and rutile-type GeO_2 (r-GeO_2) have been determined in the temperature range 7–1000 K. The harmonic effective interatomic potential $V(u) = \alpha u^2/2$ was evaluated from the contribution to the thermal vibration, where u is the deviation of the bond distance from the location of the potential minimum. The potential coefficient α for the Ge—O bond of the tetrahedron in q-GeO_2 is 24.6 eV Å^{-2}. The potential coefficients α for the four coplanar Ge—O bonds and the two axial bonds of the octahedron in r-GeO_2 are 12.9 and 14.9 eV Å^{-2}, respectively. The potential coefficient α for the second-nearest Ge—Ge distance in q-GeO_2 is 9.57 eV Å^{-2}. The potential coefficients α for the second- and third-nearest Ge—Ge distances in r-GeO_2 are 11.6 and 7.18 eV Å^{-2}, respectively. The effective interatomic potential is largely influenced by the local structure, particularly by the coordination numbers. The phonon dispersion relations for q-GeO_2 and r-GeO_2 were estimated along [100] by calculating the dynamical matrix using the potential coefficients α for the Ge—O and Ge—Ge motions. The quartz-type structure has a more complex structure with a wide gap between 103 and 141 meV and a highest energy of 149 meV, whereas the rutile-type structure has a continuous distribution and a highest energy of 126 meV.

Keywords: EXAFS; Debye–Waller factor; XANES spectra; stishovite; SiO_2 polymorphs; GeO_2 polymorphs; effective interatomic potentials; phonon dispersion relation.

1. Introduction

Extended X-ray absorption fine structure (EXAFS) spectroscopy is a useful method for structural investigation around a particular kind of atom in materials and provides important information on the thermal vibration of local structure. The Debye–Waller factor determined by EXAFS spectroscopy, which describes the attenuation of EXAFS due to the thermal motion of atoms, is sensitive to short-range correlations of the atomic motion: the mean-square relative displacement of the backscattering atoms with respect to the absorbing atom can be determined by EXAFS spectroscopy (Beni & Platzmann, 1976; Ishii, 1992). Many studies have explored the possibility that EXAFS provides an effective interatomic potential (Yokoyama *et al.*, 1989; Yoshiasa, Kamishima *et al.*, 1997; Yoshiasa *et al.*, 1998; Yoshiasa & Maeda, 1999) with a temperature-independent shape. Recently, EXAFS spectroscopy results have been utilized as a reliability test for the interatomic potentials in molecular dynamics simulations (Dalba *et al.*, 1994; Yashiro *et al.*, 1997). The feature of vibrational motion of the pair of atoms depends on the lattice type and chemical bonding (Yoshiasa, Koto *et al.*, 1997). Vibrational properties and the effective interatomic potential in materials are affected largely by the change in coordination number at a phase transition point (Yoshiasa *et al.*, 1998, 1999).

α-Quartz is an important optical and electrical material and transforms into different SiO_2 polymorphs, such as β-quartz, tridymite, cristobalite, coesite and stishovite, under high temperature and high pressure. Quartz is an important constituent in most igneous, sedimentary and metamorphic rocks. The high-temperature form, tridymite, is frequently found in groundmasses and cavities of

volcanic rocks. The high-pressure form, stishovite, is thought to be stable in the Earth's mantle. The thermodynamic and structural properties and lattice dynamics of SiO_2 polymorphs have been studied extensively (Striefler & Barsch, 1975; Barron *et al.*, 1976; Sugiyama *et al.*, 1987; Tsuneyuki *et al.*, 1988; Richet, 1990) because these polymorphs are geologically important. The densities of α-quartz, tridymite and stishovite are 2.7, 2.3 and 4.3 g cm^{-3}, respectively. In stishovite, Si is octahedrally coordinated by the O atoms while in other modifications Si is tetrahedrally coordinated.

The coordination of silicon in silicates undergoes a change from fourfold in crustal and upper-mantle minerals to sixfold in the lower-mantle minerals. These coordination changes occurred in the mantle transition zone. Many germanates adopt similar structures to silicates and undergo the same phase transitions as the corresponding silicates. The pressure-induced phase transitions in germanates occur at lower pressures than in silicates. Germanates have therefore been used as models for the corresponding silicates. In SiO_2 and GeO_2 the phase transitions accompanying a change in coordination of Si and Ge from fourfold to sixfold are achieved at 1300 K under pressures of ~9 GPa and 0.1 MPa, respectively.

Some X-ray absorption measurements near the Si *K*-edge have been performed on the amorphous and crystalline thin-film materials of silicon compounds for electronic devices (Nakano & Ogata, 1992; Nakano *et al.*, 1993). On the other hand, the precise local structure analysis and determination of EXAFS Debye–Waller factors around silicon in crystalline silicates have been seldom reported because EXAFS measurements and sample preparations for the Si *K*-edge in the soft X-ray domain are not readily available in the transmission mode. Germanium is an element which can be conveniently studied with X-ray absorption spectroscopy under high temperature and high pressure (Houser *et al.*, 1988; Yashiro *et al.*, 1997; Yoshiasa *et al.*, 1999).

In this study we attempted to determine the local structure and mean-square relative displacements of Si—O bonds in SiO_2 polymorphs and of Ge—O bonds in GeO_2 polymorphs by the EXAFS method using synchrotron radiation measurements with high-energy resolution and precision. The analysis of temperature-dependent EXAFS spectra provides information on the thermal vibration of each neighbouring atom such as the first-, second- and third-nearest-neighbour atoms. The EXAFS Debye–Waller factor allows us to evaluate the anharmonicity of effective pair potentials and the interatomic force constants for each neighbouring atom. The stretching motion of the pair of atoms is the most effective in the EXAFS Debye–Waller factor. In order to study if the interatomic force constants for each neighbouring atom change significantly with the local environment of atoms, we have determined the temperature variation of the local structural parameters in quartz- and rutile-type GeO_2 up to 1000 K. The higher parts of phonon frequencies which arise from the local structures in quartz- and rutile-type structures are discussed based on the EXAFS analysis.

2. Experimental and analysis

Single crystals of α-quartz (quartz) and α-tridymite (tridymite) were kindly provided by M. Kawasaki (Nihon Denpa Co. Ltd, Saitama) and T. Handa (Toneyama High School, Osaka). Stishovite was synthesized using a 6–8-type uniaxial split-sphere apparatus under 11.0 GPa at 1400 K. Single crystals of rutile-type GeO_2 (r-GeO_2) were synthesized under 6.1 GPa at 1300 K. Single crystals of quartz-type GeO_2 (q-GeO_2) were grown with the aid of $Li_2Mo_2O_7$ flux by slow cooling. The specimens of quartz, tridymite, stishovite, q-GeO_2 and r-GeO_2 were identified by X-ray diffraction.

The crystals of SiO_2 polymorphs were ground into fine powder using an agate mortar. A uniform fraction of grain size ~0.1–0.5 μm was separated by an elutriation method with alcohol. Very thin and homogeneous specimens of ~2 μm in thickness were obtained by sedimentation on a 2.5 μm-thick Mylar film (Chemplex Industries Inc.).

The measurements of Si *K*-edge EXAFS spectra were carried out in transmission mode at beamline BL-8B of the Photon Factory, Tsukuba. Details of the spectrometer have been given by Nakano *et al.* (1993). The distance between the X-ray source point of the storage ring and the sample is 31 m. The bent cylindrical focusing mirror is located downstream of the double-crystal monochromator in order to reduce the thermal load of the first monochromator crystal. A flat mirror is located just upstream of the X-ray measurement system to eliminate the harmonics. The synchrotron radiation beam is reduced to a size 2.0 × 0.5 mm on the specimen position. The accuracy of the photon energy is better than 0.1 eV and the energy resolution of the beamline is 0.34 eV at the energy of the Si *K*-edge with InSb(111) monochromator crystals. The current of the positron storage ring was approximately 300 mA at 2.5 GeV. Ionization chambers were applied as incident and transmission beam intensity monitors. The working gas pressure of the monitors was controlled by a diaphragm vacuum gauge, a conductance regulating valve and a proportional integral controller. Neon gas was used as the working gas with pressures of 3 kPa and 7 kPa for the incident and transmission monitors, respectively. The measured pressure fluctuation was less than 0.1%.

All X-ray absorption measurements near the Ge *K*-edge in the temperature range 7–1000 K were made at beamline BL-7C of the Photon Factory, Tsukuba. Details of the measurement are given by Yoshiasa, Koto *et al.* (1997) and Yoshiasa *et al.* (1999). The synchrotron radiation was monochromated by an Si(111) double-crystal monochromator. The appropriate amounts of fine-powder sample and boron nitride powder were mixed and pressed into pellets of 0.5 mm in thickness and 10.0 mm in diameter. All samples had edge-jumps of 0.7($\Delta\mu d$), where μ is the linear absorption coefficient and d is the thickness.

The EXAFS interference function, $\chi(k)$, was extracted from the measured absorption spectra using standard procedures (Maeda, 1987), where k denotes the wave number of photoelectrons: $k = [2m(E - E_0)/\hbar^2]^{1/2}$. $\chi(k)$ was normalized using MacMaster coefficients according to the EXAFS workshop report (Lytle *et al.*, 1989). Fig. 1 shows the X-ray absorption $\mu(E)d$ near the Si K-edge of tridymite. Fig. 2 shows the Fourier transforms of the Si K-edge EXAFS spectra for tridymite and stishovite at 300 K. In quantitative analyses we carried out the Fourier-filtering technique and a non-linear least-squares fitting method by comparing the observed $\chi(k)_{\rm exp}$ and calculated $\chi(k)_{\rm calc}$. We used the EXAFS formula in the single-scattering theory with harmonic approximation (Ishii, 1992)

$$\chi(k) = \sum_B (N_B/kR_{AB}^2)\left|f_B(k,\pi)\right| \exp[-2R_{AB}/(k/\eta)] \times \exp(-2\sigma 2k^2)\sin[2kR_{AB} + \psi_{AB}(k)],$$

where N_B is the coordination number of scattering atoms B at distance R_{AB} from the absorbing atom A, $|f_B(k,\pi)|$ is the backscattering amplitude of photoelectrons and $\psi_{AB}(k)$ is the phase-shift function. Values of the function $|f_B(k,\pi)|$ and $\psi_{AB}(k)$ were calculated using the program *FEFF3* (Rehr *et al.*, 1991). The Debye–Waller term, $\sigma 2$, indicates the mean-square relative displacement between the absorbing atom and backscattering atoms. The mean free path λ of the photoelectron is assumed to depend on the wave number, $\lambda(k) = k/\eta$, where η is a constant.

Double-shell fitting was carried out for the first-neighbour distances in the rutile-type structure, where the number of neighbouring atoms was fixed as $N_{B1} = 4$ and $N_{B2} = 2$. Single-shell fitting was applied for the first-neighbour distances in tridymite and the quartz-type structures, where the number of neighbouring atoms was fixed at the crystallographic value as $N_B = 4$. For the second- and third-neighbour distances, single-shell fitting was also carried out. Because no evident temperature dependence for η and ΔE_0 in q-GeO_2 and r-GeO_2 was revealed in this experimental resolving power, we assumed that η and ΔE_0 have negligible temperature dependence. Here, ΔE_0 is the difference between the theoretical and experimental threshold energies. The values of η and ΔE_0 for q-GeO_2 and r-GeO_2 are determined so as to give the best fit to the spectrum at 7 K. The refinement was

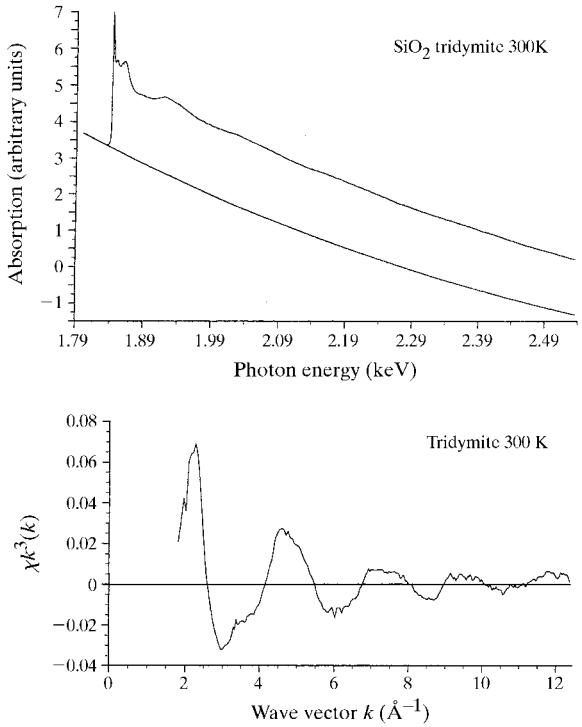

Figure 1
Observed EXAFS spectra and EXAFS oscillation near the Si K-edge of tridymite.

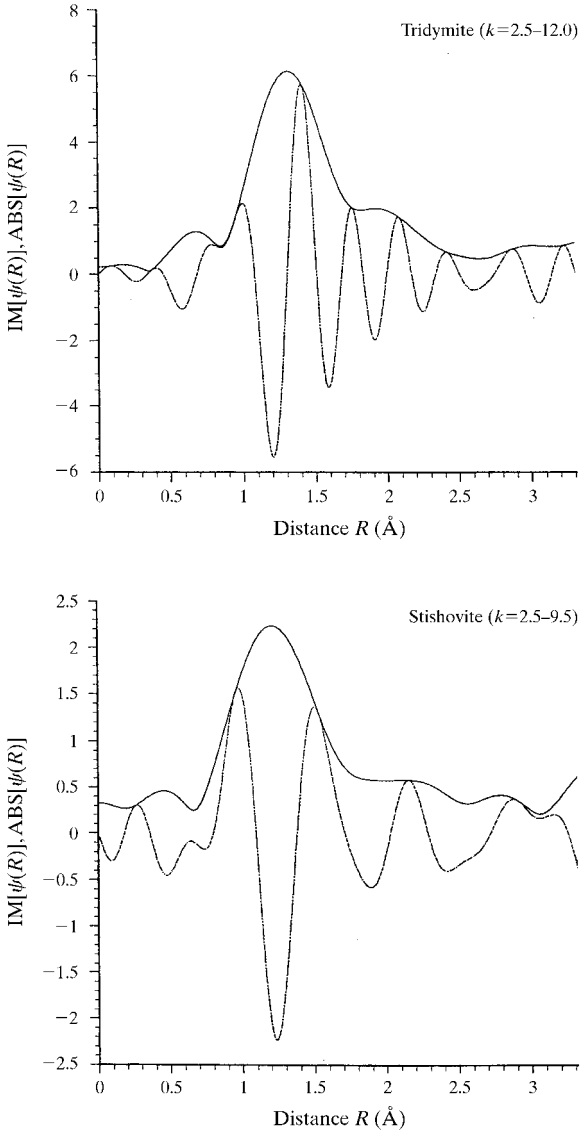

Figure 2
Fourier transforms of the Si K-edge EXAFS for tridymite and stishovite at 300 K. No phase-shift corrections are made.

performed on the structure parameters R_{AB} and $\sigma 2$ in each shell by use of the fixed η and ΔE_0 values.

On the parameter fitting, according to the EXAFS workshop report (Lytle *et al.*, 1989), the calculated EXAFS function was also filtered by the same method as was used for the observed function in order to eliminate truncation effects through the Fourier transform of the data. The equal deformation of the observed and calculated EXAFS function improves the accuracy of the parameter fitting. The reliability of fit parameters,

$$R = \sum_s \left| k_s^3 \chi(k_s)_{\rm exp} - k_s^3 \chi(k_s)_{\rm calc} \right| / \left| k_s^3 \chi(k_s)_{\rm exp} \right|,$$

between the experimental and calculated EXAFS functions was less than 0.068. The quality of fit between $k^3\chi_{\rm exp}$ and $k^3\chi_{\rm calc}$ is shown in Fig. 3.

3. Results and discussion

3.1. *XANES spectra and electronic states of polymorphs*

The X-ray absorption near-edge structure (XANES) spectra are quite sensitive to the electronic states and three-dimensional atomic configuration around X-ray absorbing atoms. The XANES spectra of quartz, tridymite, stishovite, q-GeO_2 and r-GeO_2 are shown in Fig. 4. The overall features of XANES spectra of tridymite are similar to those of quartz, but distinguishable. The XANES spectrum of stishovite differs from those of fourfold-coordinated structures. Si *K*-edge XANES spectra would be useful for distinguishing between fourfold- and sixfold-coordinated Si in silicate minerals. It can be used simply for identification of the coordination environment of atoms and of the phase transition accompanying a change in coordination numbers.

Many structural analogies on the XANES spectra exist between silicon and germanium dioxide with the same structure type. The overall features of XANES spectra of q-GeO_2 are very similar to those of quartz. The XANES spectra of sixfold-coordinated Si and Ge in the rutile-type structure are characterized by well defined features: the near-edge spectra for rutile-type structure shows discernible shoulders at both lower- and higher-energy sides of the most intense peak.

It is well known that there is a large difference in the bonding of fourfold-coordinated quartz and sixfold-coordinated stishovite. The electronic structures of quartz and stishovite were calculated and compared with experimental Si *K*- and $L_{2,3}$-edge XANES spectra (Li *et al.*, 1993). The densities of the unoccupied Si 3*s*, 3*p* and 3*d* states in the band gap and the conduction band were revealed by the XANES spectra. The most intense peak in the XANES spectra of stishovite is attributed to the transition of Si 1*s* electrons to the antibonding t_{1u} orbital (Si 3*p*-like) (Li *et al.*, 1993). The most intense peak of stishovite shifts by ~2 eV to higher energy compared with those of the fourfold-coordinated structures. In Fig. 4 the same chemical shift is observed between q-GeO_2 and r-GeO_2. The shifts towards higher energy in sixfold-coordinated rutile-type structures are caused by the different effective charges on cations,

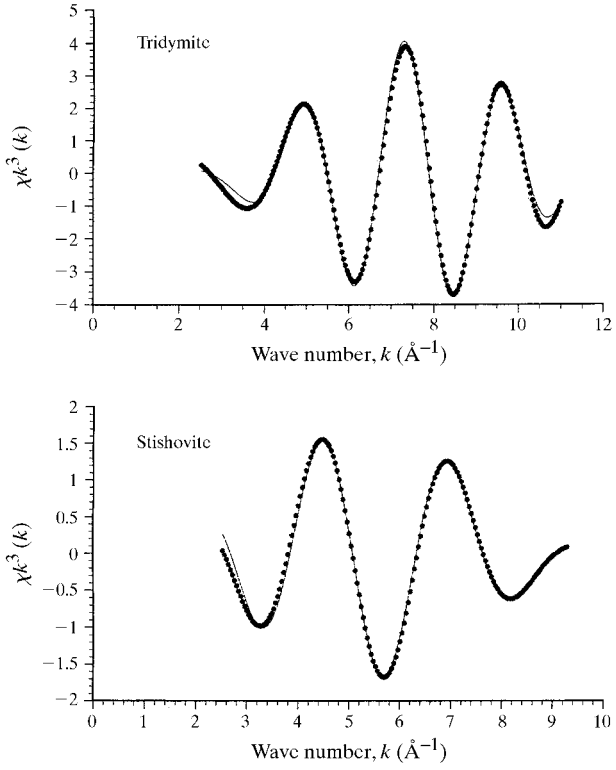

Figure 3
Fourier-filtered EXAFS spectra (dotted curve) and least-squares fits (solid curve) for first-nearest Si—O distances in tridymite and stishovite at 300 K.

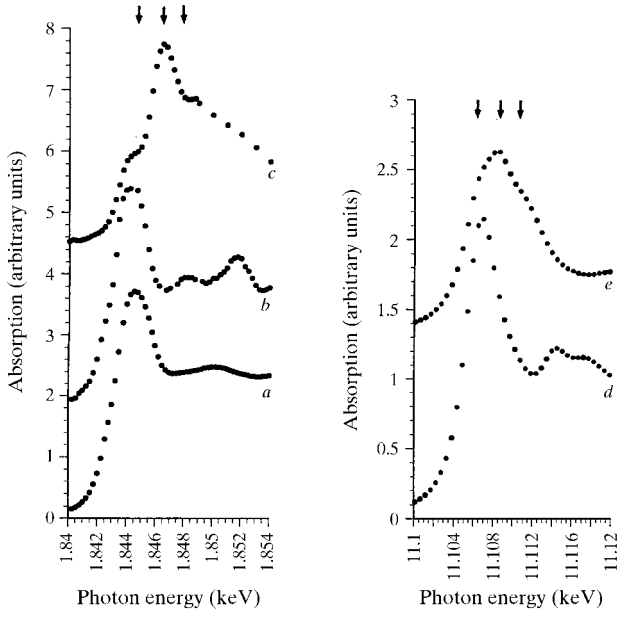

Figure 4
Experimental XANES spectra of (*a*) tridymite, (*b*) quartz and (*c*) stishovite for the Si *K*-edge region, and of (*d*) quartz-type GeO_2 and (*e*) rutile-type GeO_2 for the Ge *K*-edge region. The XANES spectra are useful for distinguishing between fourfold and sixfold coordination.

Table 1
The obtained parameters for Si—O and Ge—O bonds in SiO_2 and GeO_2 polymorphs at 300 K.

SiO_2 300 K	N	R (Å)	$\sigma 2$ (Å^2)	η (Å^{-2})	ΔE (keV)	Δk (Å^{-1})	R-factor (%)
Tridymite	4	1.597(3)	0.0031(7)	2.5(1)	0.008(1)	2.5–11.0	3.30
Quartz	4	1.618(5)	0.0023(8)	2.2(2)	0.007(1)	2.5–10.0	1.80
Stishovite	2	1.813(15)	0.0047(22)	1.9(1)	0.007(2)	2.5–9.3	6.80
	4	1.755(8)	0.0100(17)	1.9	0.014(1)		

GeO_2 300 K	N	R (Å)	$\sigma 2$ (Å^2)	η (Å^{-2})	ΔE (keV)	Δk (Å^{-1})	R-factor (%)
Qz-type	4	1.751(2)	0.0022(2)	0.32(2)	0.0023(3)	2.5–12.5	3.86
Ru-type	2	1.914(8)	0.0039(4)	0.60(3)	0.0067(5)	2.5–12.5	6.11
	4	1.866(5)	0.0044(3)	0.60	0.0078(5)		

which are related to changes of the coordination numbers of Si and Ge. These results consistently indicate the stronger covalent bonding in fourfold-coordinated structures than in sixfold-coordinated structures.

3.2. *Si—O and Ge—O distances in the polymorphs*

The obtained parameters for Si—O and Ge—O bonds in SiO_2 and GeO_2 polymorphs at 300 K are listed in Table 1. Quartz and tridymite are built up by SiO_4 tetrahedra and stishovite is isostructural with rutile with SiO_6 octahedra. The Si and Ge atoms in tridymite, quartz, stishovite, q-GeO_2 and r-GeO_2 have some first-nearest-neighbour distances which are crystallographically non-equivalent with each other. Double-shell fitting was applicable to the rutile-type structures. In the rutile-type structures, Si and Ge are octahedrally coordinated and the four coplanar bonds are shorter than the two axial bonds. The four coplanar Si—O bonds of 1.755 (8) Å in stishovite are shorter than the other two axial bonds of 1.813 (15) Å. These bond distances agreed closely with those by single-crystal structure analysis [1.7582 (1) and 1.8095 (3) Å; Sugiyama *et al.*, 1987). The single-shell fitting was carried out by least-squares calculations. The mean bond distances of 1.597 (3) Å for tridymite and 1.618 (5) Å for quartz agreed with those by single-crystal structure analysis [1.597 Å (Baur, 1977) and 1.610 Å (Zachariasen & Plettinger, 1965)]. The high-temperature phase, tridymite, has smaller local bond distances than quartz.

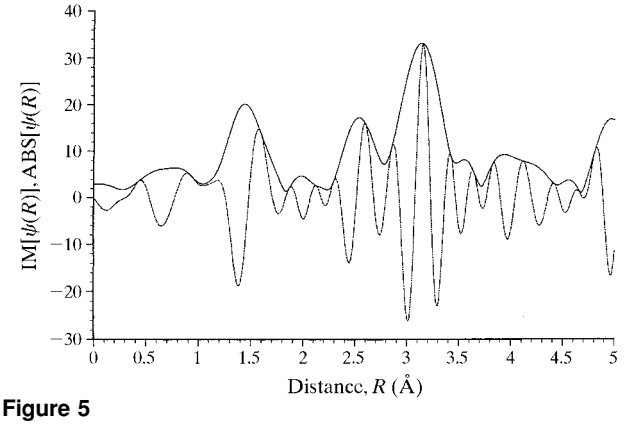

Figure 5
Fourier transforms of the Ge K-edge EXAFS for rutile-type GeO_2 at 7 K. No phase-shift correction is made.

3.3. *Temperature dependence of the Ge—Ge distance in rutile-type GeO_2*

Fig. 5 shows the Fourier transform of the EXAFS for r-GeO_2 at 7 K. The peaks corresponding to the second- and third-neighbour distances were recognizable even at 1000 K. Fig. 6 shows the temperature dependence of the Ge—Ge second- and third-neighbour distances in r-GeO_2. All second- or third-neighbour distances are crystallographically equivalent with each other. The Ge—Ge distances increase due to thermal expansion. We can determine the lattice constants using both values of second- and third-neighbour distances from the EXAFS method. The second-neighbour Ge—Ge distance is identical with the c-axis. The a-axis can be calculated using the equation $\{2[(d_{\text{third}})^2 - (d_{\text{second}}/2)^2]\}^{1/2}$, where d_{third} and d_{second} indicate the third- and second-neighbour distances, respectively. The temperature dependence of the lattice constants

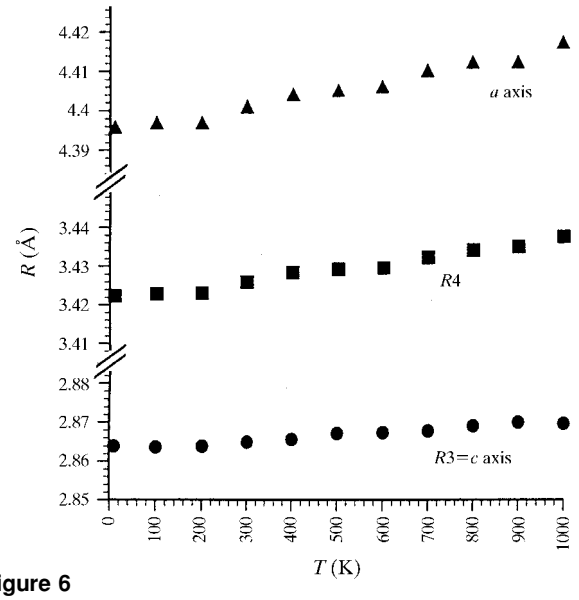

Figure 6
Temperature dependence of the second- ($R3$) and third-neighbour Ge—Ge distances ($R4$) in rutile-type GeO_2. The lattice constants **a** and **c** are determined using the values of the second- and third-neighbour Ge—Ge distances.

a and **c** are consistent with the curvature derived from the literature (Touloukian *et al.*, 1970).

3.4. *EXAFS Debye–Waller factors for Si—O, Ge—O and Ge—Ge distances*

Fig. 7 shows the temperature dependence of the Debye–Waller-type factor $\sigma 2$ for Ge—O distances in q-GeO_2 and r-GeO_2. In the low-temperature region, zero-point vibration is predominant. It is known that stishovite undergoes larger contributions to the thermodynamic functions from the zero-point vibration than quartz (Lee & Gonze, 1995). The variable $\sigma 2$ includes the effects of static and dynamic disorders. The static disorder is the configuration disorder, while the dynamic disorder arises from the thermal vibration of atoms. In addition, there is a correlation in calculation between $\sigma 2$ and the mean free path λ of the photoelectron. In the higher-temperature region the contribution of the thermal vibration, $\sigma_{thermal}$, can be estimated under the assumption of classical statistical dynamics by the temperature dependence of $\sigma 2$ (Yoshiasa *et al.*, 1999). The gradient for the experimental $\sigma 2$ in the higher-temperature region is equal to k_B/α, if we evaluate the harmonic effective interatomic potential $V(u) = \alpha u^2/2$ from the contribution to the thermal vibration, where k_B is the Boltzmann constant, α is the potential coefficient and u is the deviation of the bond distance from the location of the potential minimum. A steep slope in the figure indicates a weak bonding. The potential coefficients α for the four coplanar Ge—O bonds and for the two axial bonds of the octahedron in r-GeO_2 are 12.9 and 14.9 eV Å^{-2}, respectively. The potential coefficient α for the Ge—O bond of the tetrahedron in q-GeO_2 is 24.6 eV Å^{-2}.

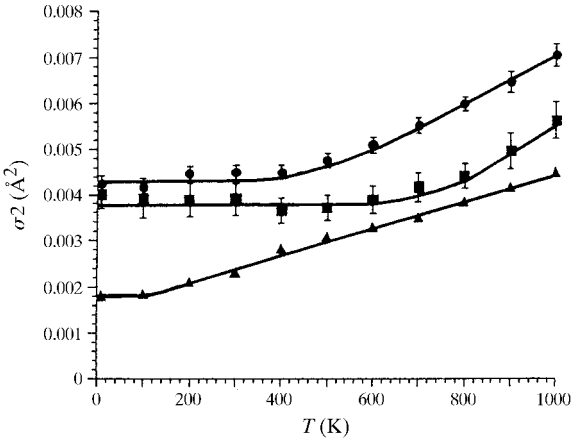

Figure 7
Temperature dependence of the Debye–Waller factor $\sigma 2$ for the Ge—O bonds of the tetrahedron in quartz-type GeO_2 (filled triangles) and for the four coplanar Ge—O bonds (filled squares) and the two axial bonds (filled circles) of the octahedron in rutile-type GeO_2.

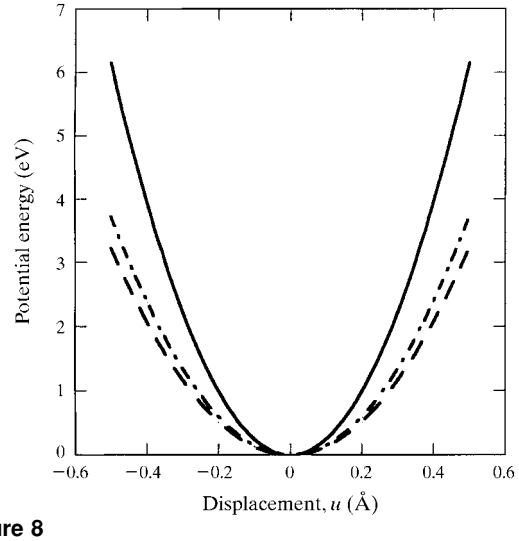

Figure 8
Effective interatomic potentials for the Ge—O bonds of the tetrahedron in quartz-type GeO_2 (straight line) and for the four coplanar Ge—O bonds (dashed line) and the two axial bonds (dash–dotted line) of the octahedron in rutile-type GeO_2.

Fig. 8 shows the effective interatomic potentials for Ge—O bonds in q-GeO_2 and r-GeO_2. We consider the vibration of Ge and O, interacting *via* a harmonic interatomic potential $V(u)$. The effective interatomic potential is largely influenced by the coordination numbers (Yoshiasa

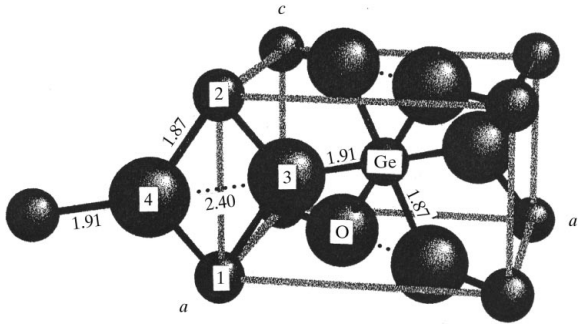

Figure 9
The rutile-type GeO_2 structure consists of GeO_6 octahedra chains. The shared edges (3–4) of the octahedron are shortening because of the reduction of the repulsive force between the Ge atoms (1–2). The distances shown are given in Å.

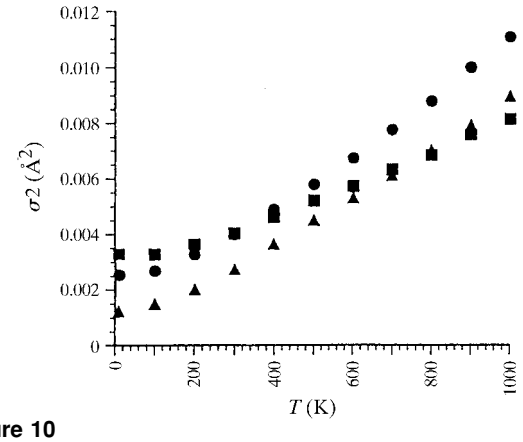

Figure 10
Temperature dependence of the Debye–Waller factor $\sigma 2$ for the second-neighbour Ge—Ge distance in quartz-type GeO_2 (filled triangles) and for second- (filled squares) and third-neighbour (filled circles) Ge—Ge distances in rutile-type GeO_2.

et al., 1998, 1999). The effective interatomic potentials for Ge—O bonds in r-GeO_2 are significantly broader than those in q-GeO_2. The potential coefficient decreases as a result of the greater bond distances. In r-GeO_2 the potential coefficient for the longer two-axial Ge—O bond of the octahedron is, however, larger than that for the four shorter coplanar Ge—O bonds. The rutile structure consists of chains of GeO_6 octahedra. Each octahedron shares a pair of opposite edges (Fig. 9). The shared edges are shortened compared with the unshared edges because of the shielding effect and consequent reduction of repulsive force (Sugiyama *et al.*, 1987) between the Ge atoms with the short second-nearest-neighbour distance along the *c*-axis. The O atom neighbour at a distance of 2.40 Å, which is short compared with twice the effective ionic radius of O, exists in the opposite direction of the longer axial Ge—O bond. The effective pair potential for the longer axial Ge—O bond is, therefore, steeper than the shorter coplanar Ge—O bond.

The effective interatomic potentials for Si—O bonds are not appreciably changed from quartz to tridymite (Table 1). The effective interatomic potentials for Si—O bonds in stishovite are significantly broader than those in tridymite and quartz as judged by each value of $\sigma 2$. The Si—O bond in sixfold-coordinated stishovite has a relatively larger mean-square amplitude of vibration than that in fourfold-coordinated structures. The structure changes in the high-pressure phase with an increase in coordination numbers and prolonged bonding distances make the bonds to first-nearest neighbours weaker (Yoshiasa *et al.*, 1998, 1999). Further experiments for SiO_2 polymorphs to determine the contribution of $\sigma_{thermal}$ from $\sigma 2$ are necessary at elevated temperature. However, EXAFS measurements near the Si *K*-edge in the soft X-ray domain are not readily available at high temperature in the transmission mode owing to a lack of adequate thin films for holding samples.

Fig. 10 shows the temperature dependence of $\sigma 2$ for second- and third-neighbour Ge—Ge distances in q-GeO_2 and r-GeO_2. Harmonic approximation can be applied up to 1000 K. The values of $\sigma 2$ from 500 to 1000 K follow a straight line. The interaction of Ge with the second-nearest Ge atoms across the shearing edges of octahedra contributes to the small temperature gradient of $\sigma 2$ for the second-nearest Ge—Ge distance (2.865 Å at 300 K) in r-GeO_2. The gradient of $\sigma 2$ for the third-nearest Ge—Ge distance (3.426 Å at 300 K) in r-GeO_2 is larger than that for the second-nearest Ge—Ge distance (3.140 Å at 300 K) in q-GeO_2. The potential coefficients α for the second- and third-nearest Ge—Ge distances in r-GeO_2 are 11.6 and 7.18 eV $Å^{-2}$, respectively. The potential coefficient α for the second-nearest Ge—Ge distance in q-GeO_2 is 9.57 eV $Å^{-2}$.

3.5. *Local structures and phonon frequencies*

Under high temperature and high pressure the determination of the high-energy phonons by the EXAFS method is of great advantage (Yoshiasa *et al.*, 1999). Low-lying modes which attribute to the long-range correlation have little effect on the EXAFS Debye–Waller factors, $\sigma_{thermal}$. Fig. 11 shows the estimated phonon dispersion relations along [100] by calculating the dynamical matrix using the potential coefficients α for the Ge—O and Ge—Ge motions. Details of the calculation were given by Kamishima *et al.* (1997). Since our model considers only the central-force interaction with first-, second- or third-nearest atoms, degeneracy of branches takes place. The dispersion relation of q-GeO_2 has no acoustic branches in the lowest energy region as shown in Fig. 11. If the O—O interaction forces are taken into account in the calculation, the acoustic branches arise and the degeneracies of the low-lying modes are lifted. The derived results refer to short-range correlation of the Ge—O and Ge—Ge motions. The overall features of calculated phonon dispersion relations for q-GeO_2 and r-GeO_2 are consistent with the estimated phonon dispersion relation for quartz (Striefler & Barsch, 1975) and the estimated phonon densities of states of quartz and stishovite by the *ab initio* calculations (Lee & Gonze, 1995). The calculated phonon energies for materials such as Ge (Yoshiasa *et al.*, 1999), CuBr (Kamishima *et al.*, 1997) and AgI (Yoshiasa & Maeda, 1999) were consistent with the values determined by inelastic neutron scattering. It seems, however, that the calculated highest optical phonon energies for Ge—O bonds in q-GeO_2 and r-GeO_2 are too large by comparison with the values anticipated by IR absorption and Raman spectra (Madon *et al.*, 1991). Because the potential coefficients are derived from the temperature gradient for the experimental $\sigma 2$, the calculated phonon energy for a strong bonding with a small temperature gradient has a relatively larger error than that for a weak bonding.

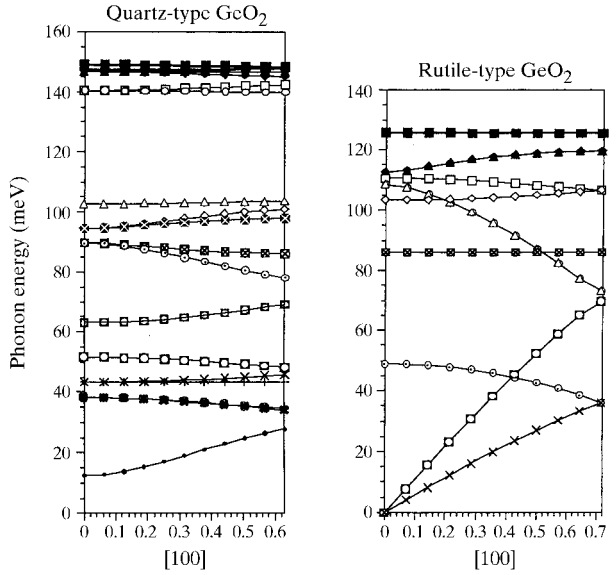

Figure 11
Calculated phonon dispersions of the quartz- and rutile-type GeO_2. The different symbols indicate individual branches.

The phonon dispersion relations of q-GeO_2 and r-GeO_2 are quite different (Fig. 11). The quartz-type structure has a more complex structure with a wide gap between 103 and 141 meV and a highest energy of 149 meV, whereas the rutile-type structure has a continuous distribution and a highest energy of 126 meV. The rutile-type structure has a significant density between 86 and 126 meV. These modes are associated with the stretching motions of Ge—O bonds in GeO_6 octahedra and the Ge—Ge stretching motion across the shearing edges of octahedra. The quartz-type structure has a significant density at lower energies with respect to that of the rutile-type structure. The quartz-type structure is characterized as softer than the rutile-type structure in the absence of the high-energy modes around 145 meV. These high-energy modes around 145 meV are associated with the stretching motion of Ge—O bonds in GeO_4 tetrahedra.

The rutile-type structure at a lower temperature has lower specific heat and lower entropy than the quartz-type structure due to the difference in the structures of the phonon dispersion relations, *i.e.* the large numbers of low-frequency vibrations give rise to an increase in vibrational entropy. The high-energy modes associated with the stretching Ge—O or Si—O motions in the GeO_6 or SiO_6 octahedra, which have lower energies than in the GeO_4 or SiO_4 tetrahedra, lead to high vibrational entropy for the rutile-type structures at a higher temperature.

This work was performed under the approval of the Photon Factory Advisory Committee (Proposal No. 95 G234).

References

Barron, T. H. K., Huang, C. C. & Pasternak, A. (1976). *J. Phys. C*, **9**, 3925–3940.
Baur, W. H. (1977). *Acta Cryst.* B**33**, 2615–2619.
Beni, G. & Platzman, P. M. (1976). *Phys. Rev. B*, **14**, 1514–1518.
Dalba, G., Fornasini, P., Gotter, R., Cozzini, S., Ronchetti, M. & Rocca, F. (1994). *Solid State Ion.* **69**, 13–19.
Houser, B., Alberding, N., Ingalls, R. & Crozier, E. D. (1988). *Phys. Rev. B*, **37**, 6513–6516.
Ishii, T. (1992). *J. Phys. Condens. Matter*, **4**, 8029–8034.
Kamishima, O., Ishii, T., Maeda, H. & Kashino, S. (1997). *Jpn. J. Appl. Phys.* **36**, 247–253.
Lee, C. & Gonze, X. (1995). *Phys. Rev. B*, **51**, 8610–8613.
Li, D., Bancroft, G. M., Kasrai, M., Fleet, M. E., Feng, X. H., Tan, K. H. & Yang, B. X. (1993). *Solid State Commun.* **87**, 613–617.
Lytle, F. W., Sayers, D. E. & Stern, E. A. (1989). *Physica B*, **158**, 701–722.
Madon, M., Gillet, Ph., Julien, Ch. & Price, G. D. (1991). *Phys. Chem. Minerals*, **18**, 7–18.
Maeda, H. (1987). *J. Phys. Soc. Jpn*, **56**, 2777–2787.
Nakano, A. & Ogata, K. (1992). *J. Mineral. Soc. Jpn*, **21**, 97–103.
Nakano, A., Ogata, K. & Nagashima, N. (1993). *Jpn. J. Appl. Phys.* **32**(S2), 70–72.
Rehr, J. J., Mustre de Leon, J., Zabinski, S. I. & Albers, R. C. (1991). *Am. Chem. Soc.* **113**, 5135–5140.
Richet, P. (1990). *Phys. Chem. Minerals*, **17**, 79–88.
Striefler, M. E. & Barsch, G. R. (1975). *Phys. Rev. B*, **12**, 4553–4566.
Sugiyama, M., Endo, S. & Koto, K. (1987). *Mineral. J.* **13**, 455–466.
Touloukian, Y. S., Kirby, R. K., Taylor, R. E. & Lee, T. Y. R. (1970). *Thermophysical Properties of Matter*, Vol. 13, *Thermal Expansion*. New York: Plenum.
Tsuneyuki, S., Tsukada, M., Aoki, H. & Matsui, Y. (1988). *Phys. Rev. Lett.* **61**, 869–872.
Yashiro, Y., Yoshiasa, A., Kamishima, O., Tsuchiya, T., Yamanaka, T., Ishii, T. & Maeda, H. (1997). *J. Phys. IV*, C**2**, 1175–1176.
Yokoyama, T., Satsukawa, T. & Ohta, T. (1989). *Jpn. J. Appl. Phys.* **28**, 1905–1908.
Yoshiasa, A., Kamishima, O., Nakatsuka, A., Ishii, T. & Maeda, H. (1997). *J. Phys. IV*, C**2**, 1173–1174.
Yoshiasa, A., Koto, K., Maeda, H. & Ishii, T. (1997). *Jpn. J. Appl. Phys.* **36**, 781–784.
Yoshiasa, A. & Maeda, H. (1999). *Solid State Ion.* In the press.
Yoshiasa, A., Nagai, T., Murai, K., Yamanaka, T., Kamishima, O. & Shimomura, O. (1998). *Jpn. J. Appl. Phys.* **37**, 728–729.
Yoshiasa, A., Nagai, T., Ohtaka, O., Kamishima, O. & Shimomura, O. (1999). *J. Synchrotron Rad.* **6**, 43–49.
Zachariasen, W. H. & Plettinger, H. A. (1965). *Acta Cryst.* **18**, 710–714.